

# Anisotropic magnetic phase diagrams, tricriticality, and spin reorientation in high-pressure grown $\text{SmCrO}_3$ single crystals

Ning Yuan,<sup>1</sup> Erik Walendy<sup>1</sup>, Nour Marayetta<sup>2</sup>, Waldemar Hergett<sup>1</sup>, Luca Bischof<sup>1</sup>, Michael Merz<sup>1,2,3,\*</sup>, and Rüdiger Klingeler<sup>1,†</sup>

<sup>1</sup>*Kirchhoff Institute of Physics, Heidelberg University, INF 227, D-69120 Heidelberg, Germany*

<sup>2</sup>*Institute for Quantum Materials and Technologies, Karlsruhe Institute of Technology, Kaiserstraße 12, 76131 Karlsruhe, Germany*

<sup>3</sup>*Karlsruhe Nano Micro Facility (KNMF), Karlsruhe Institute of Technology, Kaiserstraße 12, 76131 Karlsruhe, Germany*



(Received 7 February 2025; accepted 9 May 2025; published 21 May 2025)

$\text{SmCrO}_3$  single crystals were successfully grown utilizing the high-pressure optical floating-zone method and their crystal structure, magnetization behavior, and magnetic phase diagrams were thoroughly investigated. Magnetic studies were conducted for fields applied along all principal crystallographic directions, with measurements taken at temperatures as low as 0.4 K and magnetic fields up to 14 T. The single-crystal growth parameters are reported and the orthorhombic structure with the centrosymmetric space group  $Pbnm$  is confirmed. Long-range order of the  $\text{Cr}^{3+}$  and  $\text{Sm}^{3+}$  magnetic sublattices evolves at  $T_N = 192$  K and  $T_{N2} = 3$  K, respectively. In contrast to previous studies on polycrystals, our single-crystal data imply a discontinuous and one-step spin-reorientation (SR) of net magnetic moments  $\tilde{M}$  from the  $c$  axis into the  $ab$  plane at zero magnetic field at  $T_{SR} = 33$  K. Its discontinuous nature is maintained if  $B$  is applied parallel to the  $c$  axis but tricritical behavior and a triple point are found for  $B$  parallel to the  $a$  axis. While our data are consistent with the magnetic representation  $\Gamma_4$  for  $T > T_{SR}$ , the size and in-plane direction of the observed net magnetic moment disagree to previously proposed spin configurations, i.e.,  $\Gamma_1$  and  $\Gamma_2$ , for the spin-reoriented phases. In general, our high-quality single crystals enable us to revisit the phase diagram and to clarify the complex magnetism in  $\text{SmCrO}_3$  arising from the interplay of anisotropic  $3d$  and  $4f$  magnetic sublattices.

DOI: [10.1103/PhysRevB.111.174437](https://doi.org/10.1103/PhysRevB.111.174437)

## I. INTRODUCTION

The interplay between transition metal and rare-earth magnetic moments is highly relevant in many research areas including the important application field of permanent magnets such as Sm-Co [1,2] and Nd-Fe-B systems [3–5]. The phenomena arising especially from the interplay of  $4f$  and  $3d$  magnetic sublattices are particularly complex and give rise to a plethora of intriguing effects such as spin reorientation [6–13], solitonic lattices [14], emerging spin-phonon coupling [15], multiferroicity [16–22], spin switching [23,24], and exchange bias behavior [25]. The class of  $RCrO_3$  studied here crystallizes in a distorted perovskite-type crystal structure with space group (SG)  $Pbnm$  (which has the same symmetry as the standardized SG  $Pnma$ , yet comprises simply an alternative crystallographic setting with permuted principal axes) and two magnetic sublattices ( $R^{3+}$  and  $\text{Cr}^{3+}$ ) [26]. A main feature of the resulting magnetic interactions, among the  $3d$  moments, among the  $4f$  moments, and between  $3d$  and  $4f$  moments, is the evolution of canted antiferromagnetic order of the  $\text{Cr}^{3+}$  moments, involving a weak ferromagnetic component due to Dzyaloshinskii-Moriya interactions [27–29].

Research on rare-earth orthoferrites dates back many decades. A review of early works [30] reports the existence of three spin configurations:  $\Gamma_1$  ( $\text{Cr}^{3+}$ :  $A_x$ ,  $G_y$ ,  $C_z$ ;  $R^{3+}$ :

$O_x$ ,  $O_y$ ,  $C_z$ ) spin configuration with no net magnetic moment, while  $\Gamma_2$  ( $\text{Cr}^{3+}$ :  $F_x$ ,  $C_y$ ,  $G_z$ ;  $R^{3+}$ :  $F_x$ ,  $C_y$ ,  $O_z$ ) and  $\Gamma_4$  ( $\text{Cr}^{3+}$ :  $G_x$ ,  $A_y$ ,  $F_z$ ;  $R^{3+}$ :  $O_x$ ,  $O_y$ ,  $F_z$ ) show net magnetic moments pointing along the  $x$  and  $z$  axes, respectively (cf. Fig. S2 of the Supplemental Material (SM) [31]). The recent observations of sizable spontaneous polarization in the magnetically ordered phase triggered by the existence of high-pressure grown single crystals has renewed the interest in orthochromite research [32–34]. Whether  $RCrO_3$  serves as a potential multiferroic material remains, however, an ongoing and contentious issue. Raman studies on Sm-substituted  $\text{GdCrO}_3$  [35] reveal direct spin-phonon coupling and suggest potential applications for magnetic switching devices. Notably, clear differences appear between single-crystal and polycrystalline samples as demonstrated for  $\text{ErCrO}_3$  [36]. For the latter system a strong anomaly at the spin-reorientation transition (SRT) and the  $\text{Er}^{3+}$  magnetic ordering transition in the specific heat is only observed in studies on single crystals.

Due to the volatilization of  $\text{Cr}_2\text{O}_3$  as well as the high melting point of  $RCrO_3$  compounds, the growth of single crystals is challenging. In this work,  $\text{SmCrO}_3$  single crystals were successfully grown by the high-pressure optical floating-zone method under argon (Ar) pressure of 30 bar. The obtained single crystals have been used to investigate the magnetic and thermodynamic properties and to examine the effect of external magnetic field applied along the main crystallographic axis. While consistent with previous studies on polycrystals [25,33,37–42], long-range magnetic order of the Cr sublattice evolves at  $T_N = 192$  K. The successful synthesis of single

\*Contact author: michael.merz@kit.edu

†Contact author: klingeler@kip.uni-heidelberg.de

crystals enables us to study the SRT at  $T_{\text{SR}} = 33$  K along the principal crystallographic axes  $a$ ,  $b$ , and  $c$  individually. Applying the magnetic fields along all three crystallographic axes results in field-induced spin reorientation with critical fields varying with temperature and magnetic field direction and allows to construct the magnetic phase diagrams. We find clear differences with respect to previously reported studies on polycrystals, e.g., by following the uncompensated magnetic moment and its direction in the various magnetically ordered phases. In contrast to previous reports, our single-crystal measurements show that the SRT, at  $B = 0$  T, appears discontinuously and in a one-step transition. In addition, below  $T_{\text{SR}}$ , our data do not agree to the previously reported spin configurations. Applying magnetic fields  $B \parallel a$  drives the system towards a triple point and tricritical behavior. Distinct anomalies in the magnetization and specific heat signal the appearance of long-range magnetic order of  $\text{Sm}^{3+}$  moments at  $T_{\text{N}2} = 3$  K.

## II. EXPERIMENTAL METHODS

Polycrystalline  $\text{SmCrO}_3$  was synthesized by a standard solid-state reaction. Stoichiometric amounts of  $\text{Sm}_2\text{O}_3$  (99.9%, Alfa Aesar) and  $\text{Cr}_2\text{O}_3$  (99.6%, Alfa Aesar), along with a 10% excess of  $\text{Cr}_2\text{O}_3$ , were thoroughly mixed in a mortar and calcined at 1350°C for 48 h (air flow, ambient) with several intermediate grindings [43,44]. The obtained powder was reground, packed in a rubber tube, and isotropically pressed at 60 MPa to produce cylindrical rods with a length of 5 to 6 cm and a diameter of 5 mm. The rods were then annealed for 48 h (air flow, ambient) at 1500°C. Single crystals of  $\text{SmCrO}_3$  were successfully grown using the high-pressure optical floating-zone furnace (HKZ, SciDre) [45]. A 7-kW xenon arc lamp was used as the heat source, and a 30-bar Ar atmosphere was maintained with an Ar flow of 0.1 l/min. The feed and seed rods were pulled at a rate of 10 mm/h. To improve the homogeneity of the melting zone, counter-rotation of the feed and seed rods at 10 rpm was necessary. Further details on the growth and the sample characterization can be found in Ref. [46].

The phase purity and crystallinity of the resulting materials were studied by powder x-ray diffraction (PXRD) and the Laue method in backscattering geometry. PXRD was performed at room temperature by means of a Bruker D8 Advance ECO diffractometer using  $\text{Cu-K}\alpha$  radiation ( $\lambda = 1.5418$  Å). The data have been collected in the  $2\Theta$  range of 10°–90° with a 0.02° step size. Laue diffraction was done on a high-resolution x-ray Laue camera (Photonic Science).

The spatial structure of the prepared sample was studied by single-crystal x-ray diffraction (SC-XRD) using  $\text{Mo K}\alpha$  radiation and a resolution of 0.5 Å. Temperature-dependent SC-XRD measurements were performed at 300 and 80 K on a high-flux, high-resolution rotating anode RIGAKU Synergy-DW (Mo/Ag) system. The diffractometer is equipped with pairs of precisely manufactured Montel mirror optics, a motorized divergence slit which was set to 5 mrad for these measurements, and a background-less Hypix-Arc150° detector which guarantees the lowest reflection profile distortion and ensures that all reflections are detected under equivalent conditions. For all temperature steps nearly 12 000 Bragg

peaks were collected, significantly reducing the experimental uncertainty. The investigated sample shows no mosaic spread or additional reflections from secondary phases which demonstrates the high quality of the sample and allows for an excellent evaluation with the most recent version of the CrysAlisPro software package [47]. The data were corrected for Lorentz, polarization, extinction, and absorption effects. Using SHELXL [48,49] and JANA2006 [50], all averaged symmetry-independent reflections ( $I > 2\sigma$ ) have been included for the refinements. For both measured temperatures, the unit cell and the SG were determined, the atoms were localized in the unit cell using random phases methods, the structure was completed and solved using difference Fourier analysis, and, finally, the structure was refined.

The magnetization has been measured in a superconducting quantum interference device (SQUID) magnetometer (MPMS3, Quantum Design Inc) and in a Physical Properties Measurement System (PPMS-14, Quantum Design Inc) employing the vibrating sample magnetometer option. A relaxation method was used to perform specific heat measurements in the PPMS. When studying the temperature dependence of magnetization, zero field cooled-warming (ZFC), field cooled-cooling (FCC), and field cooled-warming (FCW) protocols were applied where the sample has been cooled down to the lowest temperature either at zero field (ZFC) before applying the external magnetic field or in the actual measurement field (FC). FC measurements have been done on warming (FCW) or cooling (FCC). Before the ZFC measurements, the applied magnetic field was zeroed-out by using the oscillation mode at room temperature.

## III. RESULTS

### A. Single-crystal growth and structure refinement

While multiple studies have been reported on the preparation of polycrystalline  $\text{SmCrO}_3$ , to the best of our knowledge, no oriented  $\text{SmCrO}_3$  single crystals have been reported which may be attributed to the challenges of heavy volatilization of  $\text{Cr}_2\text{O}_3$  and the high melting point of  $\text{SmCrO}_3$ . In many systems, the floating-zone method is considered to have an advantage in increasing the size and quality of single crystals compared to flux methods while volatilization is known to be suppressed by high Ar pressure [51–55]. This led us to investigate the crystal growth conditions for  $\text{RCrO}_3$  under high pressure. While the growth under high pressure can effectively mitigate the volatilization of  $\text{Cr}_2\text{O}_3$ , the required temperature at which the material melts will increase with pressure, approaching the operational limitation of the device. During the successful growths, *in situ* temperature measurements by means of a two-color pyrometer [53,56] determined the temperature of the melting zone to about 2300 °C.

We also observed significant amounts of deposited  $\text{Cr}_2\text{O}_3$  volatiles adhering to the inner protection glass tube, thereby affecting the focusing of light (see Fig. S1(a) of the SM [31]). Eventually it was determined by our experiments that the corresponding single crystals could be prepared at 30 bar Ar atmosphere. A relatively fast growth rate of 10 mm/h was chosen in order to further reduce  $\text{Cr}_2\text{O}_3$  volatilization. x-Ray Laue diffraction in backscattering geometry was used

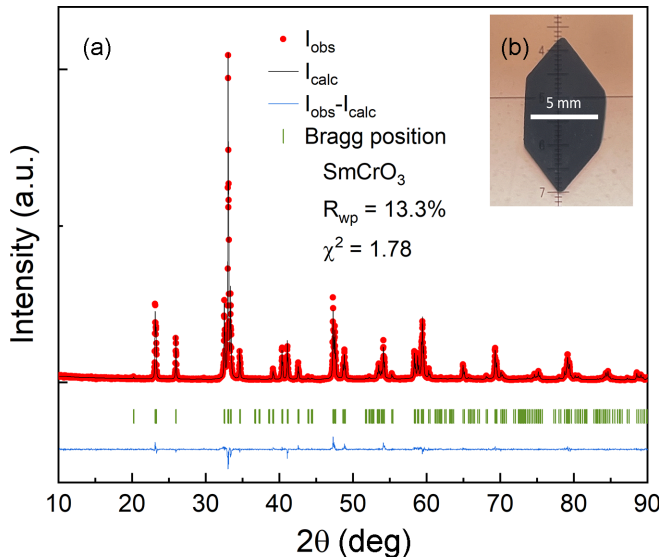


FIG. 1. (a) Room-temperature powder XRD patterns and corresponding Rietveld refinement [57] of ground  $\text{SmCrO}_3$  single crystals. The observed diffraction pattern is shown in red, the calculated one in black, and the difference between them is shown in blue. The vertical green bars show the expected Bragg positions of  $\text{SmCrO}_3$  (ICSD No. 5988 [41]). The refinement converged to  $R_{\text{wp}} = 13.3\%$  and  $\chi^2 = 1.78$ . (b) Picture of oriented single crystal used for thermodynamic measurements.

to confirm single crystallinity and to orient the single crystals which were then cut with respect to the crystallographic  $a$ ,  $b$ , and  $c$  axis using a diamond-wire saw (see Figs. S1(b) and S1(c) of the SM [31]). The powder x-ray diffraction (PXRD) on the ground  $\text{SmCrO}_3$  single crystals as well as the Rietveld refinement to the powder data are shown in Fig. 1. The result of the PXRD refinement demonstrates that the sample is free of impurity phases, and the lattice parameters and the crystal structure are consistent with previous reports [38,42,58]. Refined structural parameters are shown as Table I in the SM [31].

The quality and structure of our single crystals have been further determined by SC-XRD measurements. For the crystal structure illustrated in Fig. 2, two orthorhombic SGs were suggested in the literature and can be confirmed from our refinements: the centrosymmetric SG  $Pbnm$  (or the standardized SG  $Pnma$  see discussion above and in Ref. [38] as well as in Ref. [41]) and the noncentrosymmetric SG  $Pbn2_1$  (which is a crystallographic subgroup of  $Pbnm$  and simply an alternative setting of the standardized SG  $Pna2_1$ ) (Refs. [59] and [60]). For both measured temperatures the structure was refined in these two relevant SGs. The corresponding results of the refinements are illustrated in Table II in the SM [31]. The displacement parameters were refined anisotropically; however, due to space limitations only the equivalent ones  $U_{\text{equiv}}$  are listed in Table II. Errors shown are statistical errors from the refinement. For the 300 K as well as for the 80 K data, the structural refinements converged quite well for both suggested SGs and showed excellent reliability factors (see Table II in SM [31] for  $wR_2$ ,  $R_1$ , and GOF values). As a consequence, both proposed SGs are in principle possible. In any case, the

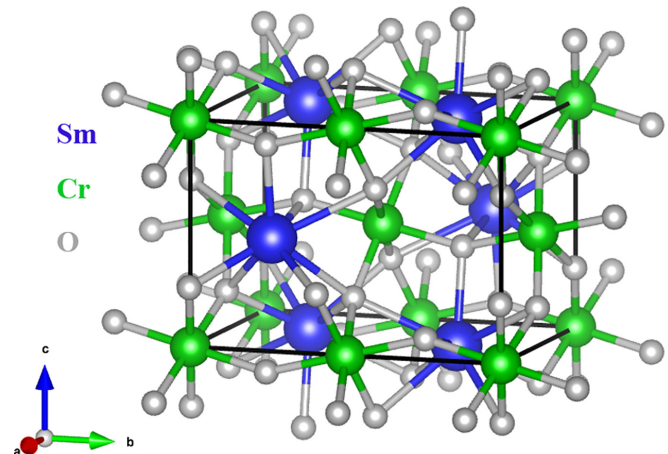


FIG. 2. Orthorhombic spatial structure of  $\text{SmCrO}_3$  at 300 K. Thin black lines represent the orthorhombic unit cell.

higher symmetry SG  $Pbnm$  shows slightly better agreement factors despite a smaller number of parameters for the atomic positions compared to the noncentrosymmetric one. Furthermore, when reducing the symmetry from  $Pbnm$  to  $Pbn2_1$  the inversion symmetry is lost but then has to reappear in the form of a twinning element which produces two merohedrally inverted twins. Therefore, the so-called Flack parameter,  $f$ , is introduced to estimate the absolute configuration of a noncentrosymmetric structural model and, thus, the respective percentage of the two inversion twins has to be refined which further increases the number of used parameters for the latter SG. The refinements of the absolute structure for SG  $Pbn2_1$  indicate that the fraction is around  $f = 50\%$  for both twins which points to the fact that the sample is either perfectly twinned or that the SG remains centrosymmetric. By taking all of the above mentioned factors into account and unless no other experiments unequivocally prove that the compound is acentric, it is generally accepted convention to use the higher symmetry and, hence, SG  $Pbnm$  has to be favored. The noncentrosymmetric refinement in SG  $Pbn2_1$  then only comes at the cost of introducing more degrees of freedom (i.e., more parameters) and even results in slightly worse agreement factors. Note that the analysis of the XRD patterns also implies that the ratio  $\text{Sm:Cr:O}_3$  (with the Sm occupation fixed to 1) very precisely amounts to 1.00:1.00:3.00, with an error in the per mille range for Sm and Cr, and less than 1% for the oxygen.

## B. Magnetic order and temperature-driven spin reorientation

The  $\text{SmCrO}_3$  single crystal reveals a pronounced magnetic anisotropy as displayed in the temperature dependence of the static magnetic susceptibility  $\chi(T) = M(T)/B$ , obtained at  $B = 10$  mT, which is shown in Fig. 3 for fields applied along the different crystallographic axes. The onset of long-range antiferromagnetic order at  $T_N = 192$  K (the phase will be labeled AF I) is associated with a pronounced increase in  $\chi_c$ , signaling the presence of a sizable net moment along the  $c$  axis as expected for canted antiferromagnetic order and in-line with previous studies on polycrystals [12,33,40]. At high temperatures, the variation of magnetic susceptibility with temperature presents a Curie-Weiss-like behavior as

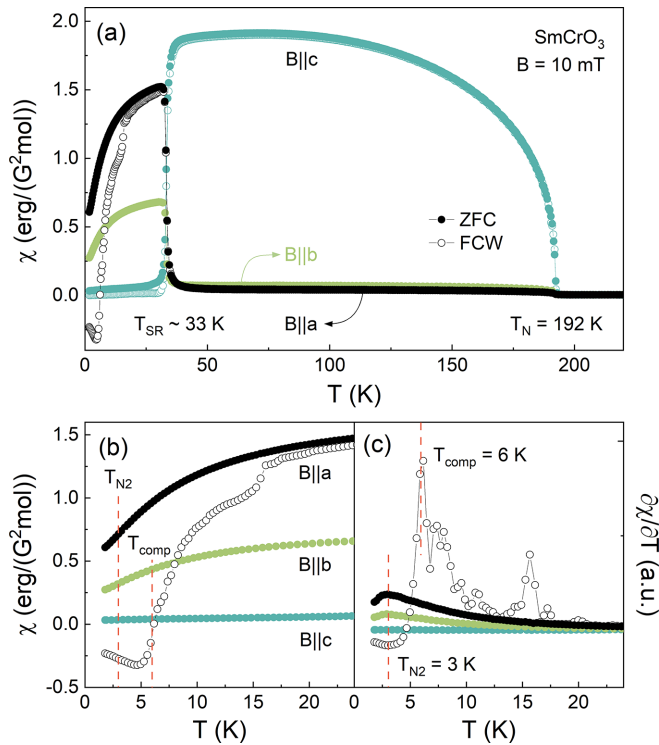


FIG. 3. (a) Temperature dependence of the static magnetic susceptibility  $\chi = M/B$ , obtained at  $B = 10$  mT applied along the crystallographic  $c$  axis ( $B \parallel c$ ),  $b$  axis ( $B \parallel b$ ), and  $a$  axis ( $B \parallel a$ ); ZFC and FCW data are represented by open and solid circles, respectively. (b) Static magnetic susceptibility and (c) its derivative for  $B \parallel c$ ,  $B \parallel b$ , and  $B \parallel a$  at  $B = 10$  mT and at  $T \leq 30$  K.  $T_N$ ,  $T_{N2}$ , and  $T_{comp}$  have been determined as described in the text.

demonstrated by  $\chi_c^{-1}(T)$  (red line) in Fig. S3 of the SM [31]. Fitting the data obtained at 1 T above 370 K by a Curie-Weiss law yields an effective moment  $p_{\text{eff}} = 3.5(1) \mu_B$  and a Weiss temperature  $\Theta_W = -373(3)$  K.<sup>1</sup> The obtained  $p_{\text{eff}}$  is lower than those reported in previous studies on polycrystalline samples [12,38,39] but closer to the theoretical value of  $3.96 \mu_B$  given by  $p_{\text{eff}} = \sqrt{p_{\text{Sm}}^2 + p_{\text{Cr}}^2}$ .<sup>2</sup> The slightly reduced value of  $p_{\text{eff}}$  might suggest that crystal fields are still relevant at 400 K, thereby affecting the  $\text{Sm}^{3+}$  moments which  $^6H_{5/2}$  ground state is likely split in three doublets (see, e.g., the discussion in Ref. [43]). In addition, the value of  $\Theta_W$  from fitting our data  $\chi(T, B = 1 \text{ T})$  above 370 K might indicate limited validity of our analysis in terms of the Curie-Weiss model which is only correct in the high-temperature regime  $T > \Theta_W$ . Our obtained  $\Theta_W$  is in particular much smaller than those reported in the literature obtained at smaller fields and lower temperatures, i.e.,  $\Theta_W = -880$  K [from a fit to  $\chi(B = 0.1 \text{ T}, T < 300 \text{ K})$ ] [12],  $-1326$  K [from  $\chi(0.05 \text{ T}, 210 - 250 \text{ K})$ ] [38], and  $-1002$  K

<sup>1</sup>The measurement field was chosen to optimize the signal-to-noise ratio while observing the low-field limit of  $B \ll B_{\text{sat}} \sim 200$  T estimated below.

<sup>2</sup>The theoretical value has been estimated by assuming  $p_{\text{eff}} = 0.845 \mu_B$  for the free-ion paramagnetic contribution of the  $\text{Sm}^{3+}$  moments ( $J = 5/2$ ) and  $p_{\text{eff}} = 3.873 \mu_B$  for  $\text{Cr}^{3+}$  moments ( $J = 3/2$ ).

[from  $\chi(0.15 \text{ T}, 210 - 250 \text{ K})$ ] [39], which may be explained by CF effects in the reported lower-temperature regimes. For comparison, we have also fitted our data by means of a Moriya model (see Refs. [28,61,62] and Fig. S3 of the SM [31]) which yields  $p_{\text{eff}} = 3.6(1) \mu_B$ ,  $\Theta_W = -435(2)$  K,  $J/k_B = 12.84(1)$  K, and  $D/k_B = 1.54(2)$  K, the latter being the symmetric and antisymmetric exchange interactions of the  $\text{Cr}^{3+}$  moments.

Upon cooling below  $T_N$ ,  $\chi_c$  reaches a maximum value of  $1.91(1)$  erg/(G<sup>2</sup>mol) at  $\sim 70$  K and then decreases sharply at  $T_{SR} \simeq 33$  K. In contrast,  $\chi_a$  and  $\chi_b$  rapidly increase at  $T_{SR}$ . The data suggest that the net magnetic moment aligns along the  $c$  axis for  $T_{SR} < T < T_N$  but rotates from the  $c$  axis into the  $ab$  plane for  $T < T_{SR}$ . Very small anomalies in  $\chi_a$  and  $\chi_b$ , at  $T_N$  (cf. Fig. 3 and the SM [31]) are in the range of uncertainty of the crystal orientation and the cutting process so that our data, for  $T_{SR} < T < T_N$ , are in agreement with the net spin component fully aligned along the  $c$  axis, i.e., with the  $\Gamma_4$  configuration.

Figure 3(b) illustrates a pronounced hysteresis between  $\chi_a$  obtained in the FC and the ZFC protocols which further confirms the presence of a weak ferromagnetic component in the  $ab$  plane at  $T \leq T_{SR}$ . Particularly,  $\chi_a^{\text{ZFC}}$  becomes zero at a compensation point around  $T_{comp} = 6$  K and has negative values at lower temperature. We attribute this to the interplay of the  $\text{Sm}^{3+}$  and  $\text{Cr}^{3+}$  magnetic sublattices. At  $T_{comp}$ , the magnetic moments of both sublattices are of equal magnitude but opposite directions, thereby canceling each other out and leading to zero magnetization and static magnetic susceptibility  $\chi$ . The persistent decrease of  $\chi_a^{\text{FCW}}$  in the low-temperature region suggests the ordering of  $\text{Sm}^{3+}$ . This is corroborated by a peak in  $\partial \chi_a / \partial T$  at  $T_{N2} = 3$  K [see Fig. 3(c) and the discussion in Sec. III C 3]. The low-temperature tail of  $\chi_a^{\text{ZFC}}$  also suggests the antiparallel arrangement of  $\text{Sm}^{3+}$  and  $\text{Cr}^{3+}$  magnetic moments. In Fig. S5 of the SM [31], the temperature hysteresis in  $\chi_a$  and  $\chi_c$  is shown for various higher magnetic fields up to 0.2 T, which demonstrates the interplay of external fields on bifurcation.

The specific heat of the  $\text{SmCrO}_3$  single crystal shown in the Fig. 4 verifies the evolution of a long-range magnetically ordered phase (AF I) at  $T_N$  and confirms a phase transition at  $T_{SR}$  into AF II. The observed anomaly at  $T_N = 192$  K is  $\lambda$  shaped which corroborates the continuous nature of the phase transition. A much sharper peaklike anomaly appears at  $T_{SR} = 33$  K and its predominantly symmetric shape indicates the first-order nature of the SRT. As will be shown below, the magnetic field  $B \parallel c$  effect on  $T_{SR}$  can be quantitatively described by the Clausius-Clapeyron equation which is valid only for discontinuous transitions and hence confirms our assignment of the nature of the transition. Finally, a broad peak in the specific heat centered around 3 K suggests a Schottky contribution to  $c_p$ .

A quantitative estimate of the anomaly at  $T_{SR}$  implies that SRT is associated with a small jump in entropy  $\Delta S_{SR} = 0.047(1) \text{ J}/(\text{mol K})$ . At  $T_N$ , one may use the anomaly size of  $5.6(25) \text{ J}/(\text{mol K})$  as an upper limit of the actual (mean-field) specific heat jump  $\Delta c_p$  since it may be superimposed by critical fluctuations. However, even this value is much smaller than the expected mean-field value for a  $S = 3/2$  system of  $\Delta c_p^{\text{mf}} = R \frac{5S(S+1)}{S^2+(S+1)^2} \simeq 18.3 \text{ J}/(\text{mol K})$ , with  $R$  being the gas

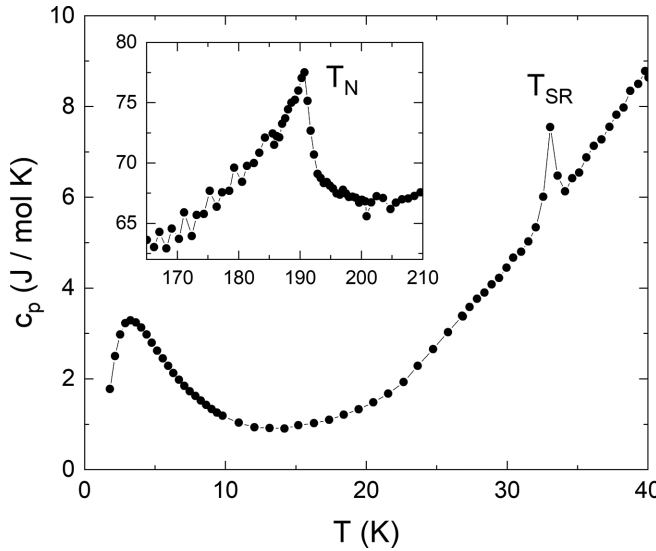


FIG. 4. Specific heat of  $\text{SmCrO}_3$  at  $B = 0$  T.  $T_N$  and  $T_{\text{SR}}$  label the onset of long-range AF order (i.e., phase AF I) of  $\text{Cr}^{3+}$  moments and SR into the phase AF II.

constant [63]. This discrepancy implies significant short-range magnetic order above  $T_N$  and/or incomplete long-range order below  $T_N$ .

The rotation of a small ferromagnetic moment from the  $c$  axis towards the  $ab$  plane is confirmed by isothermal magnetization data in Fig. 5. At  $T = 1.8$  K,  $M_a$  ( $M_b$ ) evidences a small remanent moment of  $0.013 \mu_B/\text{f.u.}$  ( $0.005 \mu_B/\text{f.u.}$ ) and a hysteresis of about  $0.1$  T ( $0.14$  T). In contrast, no sizable net moment is seen in  $M(B||c)$ , which confirms the rotation of the net magnetic moment perpendicular to the  $c$  axis at  $T_{\text{SR}}$ . The response of the net moment is superimposed by a linear-in-field increase of  $M$  which implies AF behavior. At  $B = 7$  T field,  $M_c < M_b \simeq M_a/2$ , all being much smaller than the saturation magnetization. Extrapolating  $M_a$  suggests a saturation field  $B||a$  of nearly  $200$  T.

At  $T = 20$  K, there is a steplike feature in  $M(B||c)$  which is signalled by a peak in  $\partial M/\partial B_{||c}$  at  $B_c = 6.4(1)$  T [see Fig. 5(b)]. While such a feature is not present for the other field directions at  $20$  K, it appears at  $T = 40$  K in  $M(B||a)$ , at  $B_a = 2.3(1)$  T, but at this temperature it is quenched in  $M(B||c)$  [Fig. 5(c)]. We attribute the steplike increase in magnetization to field-induced SRT from the  $ab$  plane to the  $c$  axis in the SRT phase (AF II) at  $T < T_{\text{SRT}}$ . Conversely, the field-driven rotation appears from the  $c$  to the  $a$  direction in the high-temperature phase AF I at  $T > T_{\text{SRT}}$ .

In order to further elucidate the reorientation process, we have performed a series of  $M$  vs  $B$  measurements for  $B||c$  and for  $B||a$ , respectively, at different temperatures (see Fig. 6). Similarly to the trend observed at  $1.8$  K in Fig. 5, the data for  $B||c$ , at  $10$  K display rather linear behavior typically expected for antiferromagnets at low magnetic fields. While a rather rectangular open hysteresis loop is observed for  $T > T_{\text{SR}}$ , no such hysteresis is observed at  $T \lesssim T_{\text{SR}}$ . There is, however, a tiny hysteresis-free  $\mathbb{S}$  shape of the curve  $M(B||c)$  in the field range  $|B| \leq 0.2$  T at  $T \lesssim T_{\text{SR}}$ , which points to a small magnetic moment and suggests a derivation of the pure

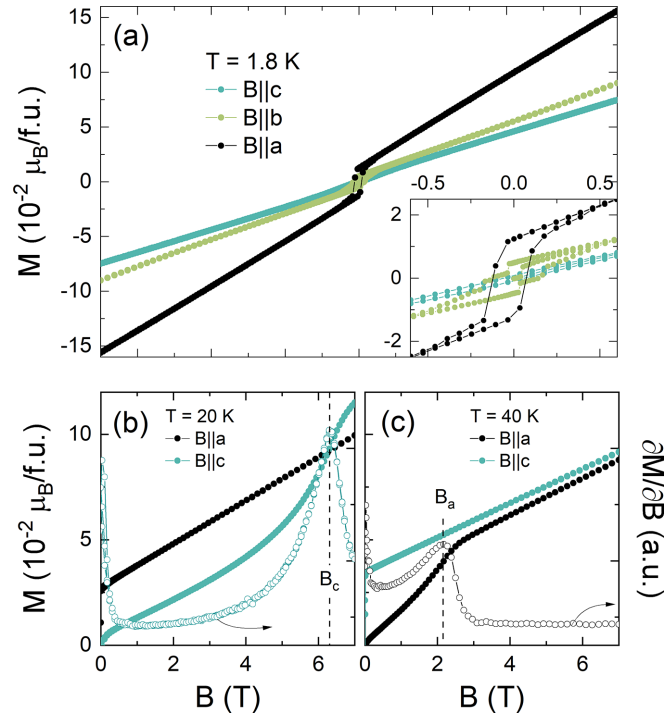


FIG. 5. (a) Isothermal magnetization at  $T = 1.8$  K for  $B||a$ ,  $b$ , and  $c$  axes. The inset highlights the behavior around zero field. (b) Isothermal magnetization at  $T = 20$  K for  $B||c$  (left ordinate) and corresponding magnetic susceptibility  $\partial M/\partial B_{||c}$  (right ordinate), and (c) the same quantities at  $T = 40$  K for  $B||a$ . The dashed lines indicate the critical field  $B_c$  and  $B_a$  as described in the text.

$\Gamma_2$  configuration. Concomitantly, a weak ferromagnetic open hysteresis curve appears for  $B||a$ . From the data in Figs. 6 and S7 of the SM [31] we extract remanent magnetic moments  $M_r^a$ ,  $M_r^b$ , and  $M_r^c$  which clearly illustrate the rotation of the weak net moments at the SRT [see Fig. 7(a)]. In particular, our single-crystal data imply the rotation of the net moment into the  $ab$  plane.

For  $T > T_{\text{SR}}$  (AF I) the measured  $\chi_c \times B$  is approximately equal to the total net magnetic moment  $\tilde{M}$  in the system. Whereas, for  $T < T_{\text{SR}}$  (AF II) the measured values  $\chi_a \times B$  ( $\chi_b \times B$ ) can be considered as the projection of  $\tilde{M}$  on the  $a$  ( $b$ ) axis. The fact that we observe finite  $M_r^a$  and  $M_r^b$  implies that  $\tilde{M}$  is not aligned along one of the crystallographic axes. From our data the angle  $\alpha$  between the  $a$  axis and  $\tilde{M}$  just below  $T_{\text{SR}}$  can be estimated to be approximately  $30^\circ$ . It visibly decreases only below  $T_{\text{N}2}$ . Furthermore, the temperature dependencies of  $M_r^a$  and  $M_r^c$  allow us to calculate the temperature dependence of the rotation angle  $\theta$ , thereby further illustrating the rotation of the net magnetic moments by utilizing the formula [64]:

$$\theta = \arctan \left( \frac{M_r^a}{M_r^c} \right). \quad (1)$$

The resulting temperature dependence is shown in Fig. 7(b). In addition,  $\theta$  can be also estimated from  $\chi_c/\chi_a$  as shown in Fig. 7(b), too. The two estimates agree perfectly to each other if the bare remanent moment is considered (data not shown). The slight deviations in Fig. 7(b) (open/filled circles around  $25$  K) are directly associated to the fact that the

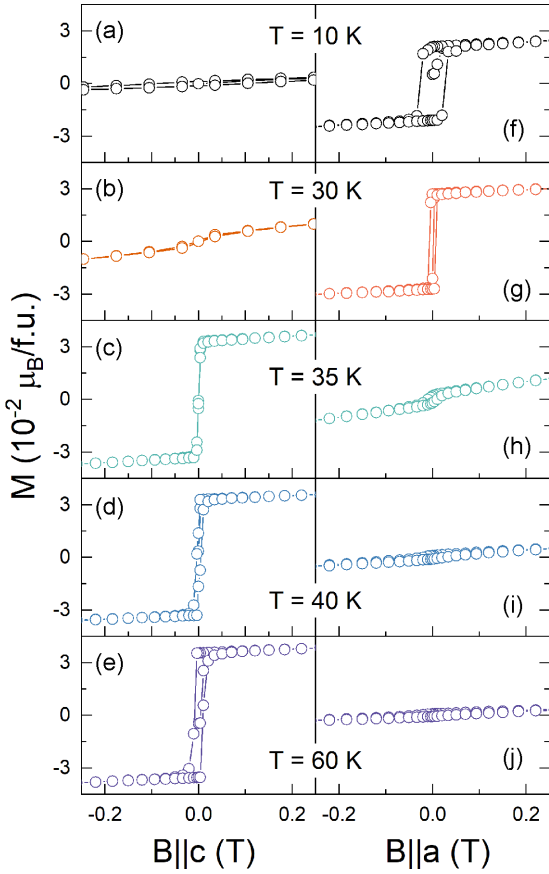


FIG. 6. Isothermal magnetization at selected temperatures for [(a)–(e)]  $B||c$  axis and [(f)–(j)]  $B||a$  axis. Data for  $B||b$  are shown in the SM [31].

small magnetic moments indicated by the S-shaped behavior in  $M$  vs  $B$  are naturally not captured by the low-field static magnetic susceptibilities  $\chi_a$  and  $\chi_c$ . As sketched in the inset of Fig. 7(b), the angle  $\theta$  characterizes the rotation of the magnetic moment in the  $ac$  plane, whereas the actual rotation plane of  $\tilde{M}$  might be approximated by the purple plane illustrated in Fig. 7(b). Thus,  $\theta = 90^\circ$  merely represents the alignment of the magnetic moment in the  $ab$  plane. Taken together, the weak ferromagnetic moments are predominantly aligned along the  $c$  axis when  $T > T_{\text{SR}}$  implying the spin configuration  $\Gamma_4$ . For  $T < T_{\text{SR}}$  the magnetic moments rotate from the  $c$  axis to the  $ab$  plane which is consistent with the  $\Gamma_2$  phase. The completely i.e., in-plane, net moment agrees very well to the net moment  $\parallel c$  just above  $T_{\text{SR}}$  [Fig. 7(a)]. The presence of such an uncompensated moment is likely attributed to a canting of the predominantly antiferromagnetic spin arrangement and in particular rules out the collinear antiferromagnetic structure  $\Gamma_1$ . On the other hand, the data also suggest a tiny remaining moment  $\parallel c$  as demonstrated by the S-shaped behavior of  $M(B||c)$ , thereby indicating deviations of  $\Gamma_2$ . Moreover, the in-plane net moment direction deviates by  $\sim 60^\circ$  from the  $b$  axis. These observations do not agree to the pure  $\Gamma_2$  case. Hence, our data imply the necessity to reassess the recent controversy whether, at low temperatures,  $\text{SmCrO}_3$  exhibits the collinear spin configuration  $\Gamma_1$  [41] or  $\Gamma_2$  [38,65]. While our data clearly rule out  $\Gamma_1$  even at low

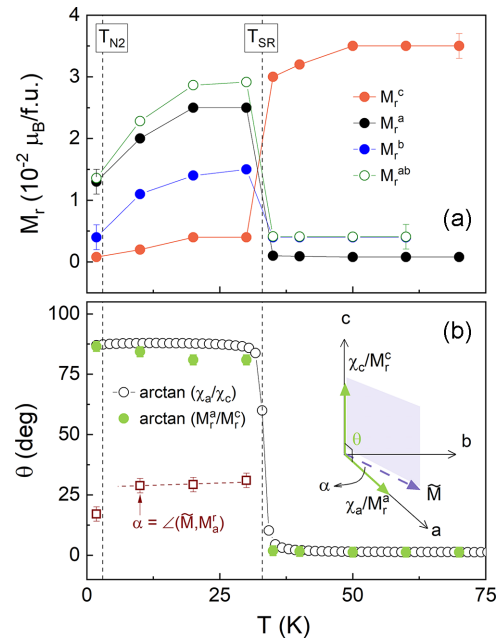


FIG. 7. (a) Temperature dependence of the remanent magnetic moment  $M_r^i$  along the three crystallographic axes  $i = a, b, c$  read-off from Figs. 6 and S7 of the SM, and calculated in-plane net moment  $M_r^{ab} = \sqrt{(M_r^a)^2 + (M_r^b)^2}$ . Error bars include systematic uncertainties associated with the crystal orientation. (b) Rotation angle  $\theta$  calculated from  $M_r^a$  and  $M_r^c$  (green circles) and from the static magnetic susceptibility  $\chi = M/B$  obtained at  $B = 0.01$  T for  $B||a$  and  $B||c$  (black circles). The sketch illustrates  $\alpha$  (shown by open squares),  $\theta$  and  $\tilde{M}$ . Vertical dashed lines mark the SRT and  $T_{N2}$ .

temperatures, the results are also inconsistent with the pure  $\Gamma_2$  representation. Additional measurements, such as neutron diffraction on single crystals, are required to clarify this issue. In addition, our single-crystal data imply that the in-plane direction of  $\tilde{M}$  is in between  $a$  and  $b$  but rotates slightly (by  $\sim 10^\circ$ ) when long-range order of the  $\text{Sm}^{3+}$  finally evolves [see Fig. 7(b)].

### C. Magnetic phase diagrams

Clear anomalies in the field and temperature dependence of the magnetization allow us to construct the magnetic phase diagrams for magnetic fields applied along the different crystallographic axes. This is illustrated for selected temperatures in Fig. 8 where for  $B||a$  and  $B||c$ , respectively, the magnetization features a jump-like increase as also indicated by the peak in isothermal magnetic susceptibility. At  $T = 25$  K, magnetic fields  $B||c$  induce a small ferromagnetic moment at  $B_c \simeq 3.9$  T [Fig. 8(a)]. For  $T > T_{\text{SR}}$ , we do not observe such a feature for  $B||c$ . We associate the anomaly with field-induced SR towards the  $c$  axis, i.e., the transition from AF II to AF I. However, similar features are seen for  $B||a$  for  $T_{\text{SR}} \leq T \leq T_N$  as illustrated by the example in Fig. 8(b). This is shown for the whole temperature regime in Figs. 9(a) and 9(b), which shows that  $B_a$  is increasing on heating above  $T_{\text{SR}}$  to a maximum of nearly 5 T, at around 55 K, while again decreasing up  $T_N$ . On the other hand,  $B_c$  continuously increases towards lower temperatures and leaves the accessible field range below 8 K [Fig. 9(c)].

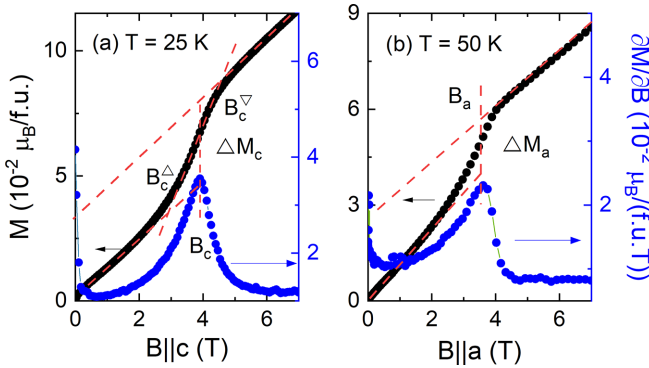


FIG. 8. Isothermal magnetization and differential magnetic susceptibility for (a)  $B||c$ , at 25 K ( $< T_{SR}$ ; AF II), and (b) for  $B||a$ , at 50 K ( $> T_{SR}$ ; AF I). Anomalies are associated with field-induced SRT.  $B_a$  and  $B_c$  are the transition fields, and  $\Delta M$  is the associated jump in magnetization.

The magnetic phase diagrams for  $B||a$  and  $B||c$  are constructed from the zero field data in Sec. III B and the critical fields,  $B_c$  and  $B_a$ , as shown above. In addition, our magnetization measurements allow us to follow  $T_N(B)$  and  $T_{N2}(B)$  as shown in Fig. S4(a) of the SM [31]. The resulting phase

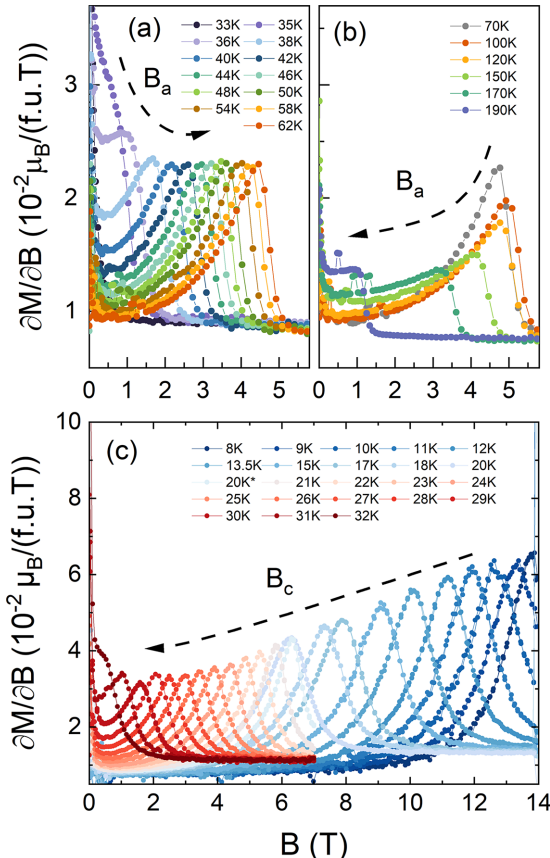


FIG. 9. Isothermal magnetic susceptibility  $\partial M / \partial B$  at various temperatures for [(a) and (b)]  $B||a$  and (c)  $B||c$ . The temperature evolution of the SRT is indicated by dashed arrows.  $\partial M / \partial B$  measured in the VSM magnetometer ( $T \leq 20$  K) have been scaled to the SQUID data ( $T \geq 20$  K) such that the anomaly heights at 20 K coincide.

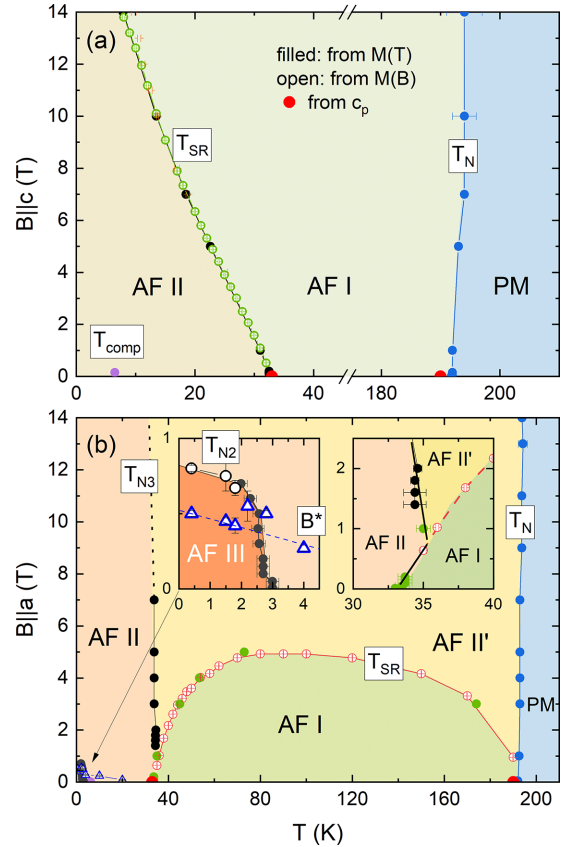


FIG. 10. Magnetic phase diagram of  $\text{SmCrO}_3$  for (a)  $B||c$  and (b)  $B||a$ . (See data for  $B||b$  in the SM) Insets in (b) highlight the regimes around 35 K and  $T_{N2}(B)$ . PM: Paramagnetic phase; AF I: AFM phase with net magnetic moments along the  $c$  axis ( $\Gamma_4$ ); AF II and II': AFM phases with net magnetic moments within the  $ab$  plane; AF III: AFM phase with ordering of  $\text{Sm}^{3+}$  moments. Labels of the phase boundaries ( $T_N$ ,  $T_{SR}$ ,  $T_{comp}$ ,  $T_{N2}$ ,  $T_{N3}$ ,  $B^*$ ) are explained in the text.

diagrams are presented in Fig. 10. In addition to the features discussed above, we also note a steep phase boundary  $T_{N3}(B||a)$  as indicated by anomalies in  $M(T, B||a > 1.5$  T) (see Figs. 10 and 12). For  $B||b$ , the magnetic phase diagram is similar to what is found for  $B||a$  and shown in Fig. S4 of the SM [31]. In the following, we discuss the main findings of the obtained phase diagrams.

For  $B||c$ , we observe an increase of  $T_N$  in the whole field range under study. The positive slope  $\partial T_N / \partial B$  agrees to the fact that the evolution of phase AF I is associated with an increase of magnetization. The absence of pronounced anomalies in magnetic susceptibility for  $B \perp c$ , on the other hand, agrees to the fact that  $T_N$  is rather independent on  $B||a$  and  $B||b$  (see Fig. 10(b) and S4 of the SM [31]). Quantitatively, the slope of the continuous phase boundary [63,66] is linked to the associated jumps in the heat capacity ( $\Delta c_p$ ) and the temperature derivative of the magnetization [ $\Delta(\partial M / \partial T)|_B$ ] as given by the Ehrenfest relation:

$$\frac{\partial T_N}{\partial B} = -T_N \frac{\Delta(\partial M / \partial T)|_B}{\Delta c_p}. \quad (2)$$

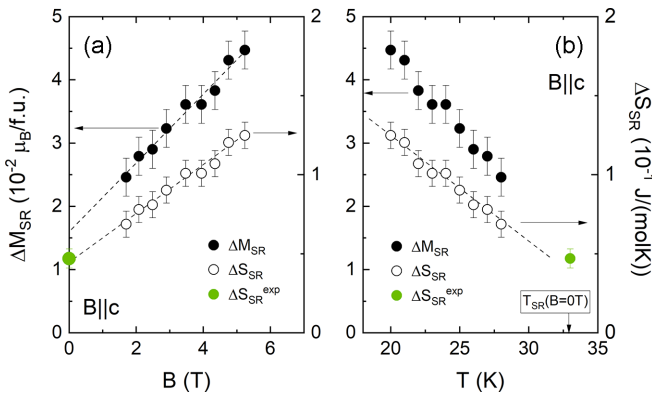


FIG. 11. Dependence of magnetization anomaly  $\Delta M_{\text{SR}}$  at the SRT (AF I  $\leftrightarrow$  AF II) extracted from the data as illustrated in Fig. 8 and associated entropy jump  $\Delta S_{\text{SR}}$  obtained by means of Eq. (3) on (a) the magnetic field  $B||c$  and (b) on the temperature, at different  $B||c$ . Dashed lines are guides to the eye. Green data markers show  $\Delta S_{\text{SR}}$  from the specific heat measurement.

From Fig. 3 we obtain the jump in  $\partial M / \partial T$ , at  $B = 0.01$  T of  $9(5) \times 10^{-4} \mu_B/\text{f.u.}$  for  $B||c$ , and  $15(3) \times 10^{-2} \mu_B/\text{f.u.}$  for  $B||a$ . Using the experimentally determined jump in the specific heat  $\Delta c_p$  from Fig. 4, Eq. (2) yields  $\partial T_N / \partial B_{||c} = 0.17(13) \text{ K/T}$  and  $\partial T_N / \partial B_{||a} = 3(1) \text{ mK/T}$ . This agrees to the observed negligible slope  $\partial T_N / \partial B_{||a}$  and, within error bars, to  $\partial T_N / \partial B_{||c} \simeq 0.28(5) \text{ K/T}$  derived from the phase diagrams in Fig. 10.

#### First-order nature of the spin-reorientation transition

In the literature, there is a controversy about the nature of the SRT in  $\text{SmCrO}_3$ . Based on polycrystal samples, Sau *et al.* [39] reported that the SRT appears in two steps, i.e., a continuous rotation followed by a discontinuous jump, with the former being of second-order and the latter of first-order nature. As shown in Figs. 4 and 3, distinct and single anomalies in our zero field measurements on the single crystal at hand do not support a two-step scenario. The one-step scenario is further corroborated by the following thermodynamic considerations: As shown in Fig. 10, magnetic fields  $B||c$  yield a monotonous suppression of  $T_{\text{SR}}$ , i.e., AF I is stabilized over the spin-rotated low-temperature phase AF II. Microscopically, this is associated with rotation of the weak net magnetic moments of the canted  $\text{Cr}^{3+}$  sublattice from the  $ab$  plane (AF II) to the  $c$  axis (AF I). For a discontinuous phase transition, the slope of the phase boundary is governed by the jumps in magnetization ( $\Delta M_{\text{SR}}$ ) and in the entropy ( $\Delta S_{\text{SR}}$ ) as described by the Clausius-Clapeyron equation [63]:

$$\frac{\partial T_{\text{SR}}}{\partial B} = -\frac{\Delta M_{\text{SR}}}{\Delta S_{\text{SR}}}. \quad (3)$$

The measured slope of the phase boundary  $T_{\text{SR}}(B||c)$  and magnetization jumps  $\Delta M$  hence enable us to calculate the associated entropy changes. The temperature and magnetic field dependence of the experimentally obtained anomaly sizes  $\Delta M_{\text{SR}}$  and the by Eq. (3) calculated entropy jumps are shown in Fig. 11. Extrapolating the results  $\Delta S_{\text{SR}}(B||c)$  in Fig. 11 to zero field in particular yields  $\Delta S_{\text{SR}} = 0.045(10) \text{ J/(mol K)}$  which nicely agrees to the experimentally measured entropy

jump of  $\Delta S_{\text{SR}} = 0.047(1) \text{ J/(mol K)}$  derived from the specific heat data in Fig. 4 (see the green data point in Fig. 11).

The fact that the entropy jump calculated by the Clausius-Clapeyron equation quantitatively agrees to the experimentally measured discontinuity confirms the measured data and in particular verifies the discontinuous nature of the SRT. We hence exclude the suggested two-step scenario for  $B = 0$  T. In addition, Fig. 11 shows that on application of  $B||c$  both  $\Delta M_{\text{SR}}$  and  $\Delta S_{\text{SR}}$  strongly increase. This implies that magnetic order in AF I is stronger suppressed in favor of the larger magnetization  $M_c$  than in AF II.

#### Tricritical and triple point for $B||a$

In contrast to the monotonous and rather constant suppression of  $T_{\text{SR}}(B||c)$ , AF I forms a dome in the phase diagram if  $B$  is applied along the crystallographic  $a$  direction (the same holds for  $B||b$ , see Fig. S4 in the SM). As shown in Fig. 10(b), AF I is stabilized with respect to AF II' for  $T \gtrsim 70$  K while being suppressed below and completely vanishes at  $T_{\text{SR}}(B = 0 \text{ T}) = 33$  K. However, the behavior for  $B||a$  is rather complex: At temperatures around  $\simeq 36$  K, the transition AF II'  $\leftrightarrow$  AF I is associated to a jump in  $\partial M / \partial B$  and, for  $B||a \gtrsim 2$  T, a kink in  $M(T)$  (see Figs. 9, S8, and S12) which implies its *continuous* nature while we recall the discontinuous transition AF II  $\leftrightarrow$  AF I at  $T_{\text{SR}}(B = 0 \text{ T})$ . The continuous nature of the AF I/AF II' phase boundary is further confirmed by clear failure to describe the slope  $T_{\text{SR}}(B||a)$  by means of Eq. (3) if anomalies are interpreted as discontinuities.

In addition to this continuous-type phase boundary separating AF I and AF II', for  $B||a > 1.5$  T we observe a small jump-like increase of  $M(T)$  which is nearly independent on  $B$  [Fig. 12(b)]. Our data hence indicate a triple and—as the jump implies the first-order character of this AF II/AF II' phase boundary—a tricritical point at  $\simeq 34$  K and  $B||a \simeq 1$  T separating phases AF I (moments  $||c$ ), AF II and AF II'. Both latter phases are characterized by moments in the  $ab$  plane, with a slightly larger net moment along  $a$  in AF II'.

The transition from AF II' to AF II is associated to finite entropy changes which lower limit can be derived utilizing the anomaly in  $M$  and the slope  $\partial T_{\text{N3}} / \partial B$  using Eq. (3). For example, the magnetization jump at  $T_{\text{N3}}(3 \text{ T})$  is of the order of  $\Delta M_{\text{N3}} \simeq 3 \times 10^{-4} \mu_B/\text{f.u.}$  The steep slope of  $T_{\text{N3}}(B||a)$  analyzed by means of Eq. (3) hence implies  $\Delta S_{\text{N3}} \gtrsim 20 \text{ mJ/(mol K)}$ .

#### Magnetization compensation and order of $\text{Sm}^{3+}$ moments

While the  $\text{Sm}^{3+}$  sublattice remains paramagnetic (but polarized by the  $\text{Cr}^{3+}$  sublattice) at  $T_N$ , ordering of the 4f moments has been reported at  $T_{\text{N2}} \simeq 4$  K as deduced from thermodynamic and neutron data [37,38,67]. However, while neutron data at 1.5 K have shown the presence of long-range  $\text{Sm}^{3+}$  magnetic order, the transition was previously [37] associated with a broad hump in the specific heat similar to what is seen in our data (Fig. 4). Such a broad hump is, however, not a typical signature of a thermodynamic phase transition but usually signals the expected Schottky contribution so that, in contrast to Ref. [37], we do not consider it evidencing  $T_{\text{N2}}$ . Contrarily, we conclude that the evolution of long-range

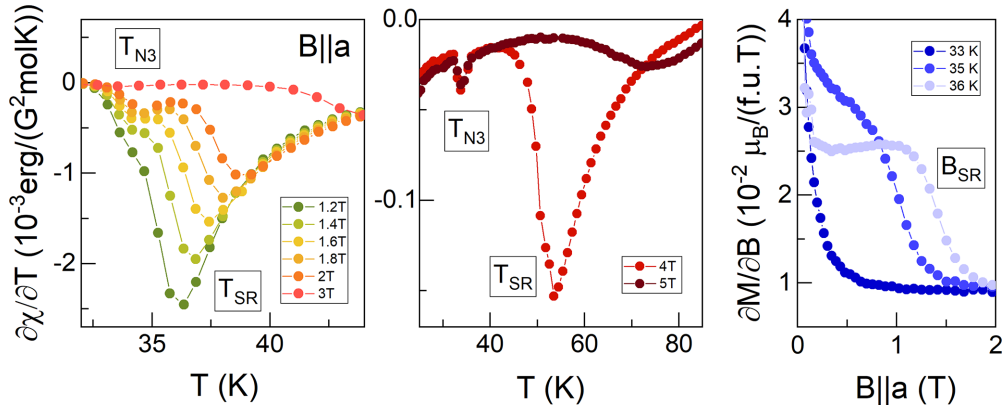


FIG. 12. Anomalies in [(a) and (b)]  $\partial\chi_a/\partial T$  and (c)  $\partial M/\partial B|_a$  for selected temperatures and fields to illustrate the  $B \parallel a$  dependence of  $T_{SR}$  and the phase boundaries between AF I, AF II', and AF II. Labels match those in the phase diagram Fig. 10. For additional data see the SM [31].

magnetic order of the  $\text{Sm}^{3+}$  sublattice from the AF II phase (where  $\text{Sm}^{3+}$  moments are highly polarized) is not associated with significant entropy changes and cannot be detected in the specific heat data against the background of the Schottky peak. In an attempt to estimate an upper limit of the expected specific anomaly by exploiting Eq. (2), we find  $\Delta c_p^{\text{TN2}} \simeq 60$  mJ/(mol K) which is clearly indistinguishable from the strong Schottky anomaly dominating the total specific heat at  $T_{N2}$  (see Fig. 4).

A characteristic feature of long-range  $\text{Sm}^{3+}$  magnetic order, however, is visible in the temperature dependence of the susceptibility which shows a small kink in  $\chi_a$  and thus a peak in  $\partial\chi_a/\partial T$  [see Fig. 13(a)]. The kinklike feature confirms the continuous nature of the phase transition. At  $B = 10$  mT ( $\parallel a$ ), the peak in  $\partial\chi_a/\partial T$  appears at  $T_{N2} \simeq 3$  K which we

interpret as the ordering temperature of  $\text{Sm}^{3+}$  moments. The field dependence of  $T_{N2}$  can be followed by the characteristic maximum in  $\partial\chi_a/\partial T$  as shown in Figs. 13(a)–13(c)]. We observe a suppression by  $\simeq 1$  K in  $B \parallel a = 0.7$  T while for higher fields the peak is not observed (see also Figs. S16 and S17 of the SM [31]). The isothermal magnetization  $M(B \parallel a)$  is dominated by the small hysteresis around  $B = 0$  T. However, we observe small additional peaks as illustrated by the data taken at  $T = 400$  mK in Figs. 13(d) and S10. Specifically, we observe a tiny hump in  $\partial M/\partial B$  both in up and down sweeps which agrees to the phase boundary  $T_{N2}(B \parallel a)$ . While this feature [labelled  $B_{N2}$  in Fig. 13(d)] vanishes at 2 K, there is a further anomaly [ $B^*$  in Fig. 13(d); see the triangles in the left inset of Fig. 10] which appears only after applying high magnetic field in the opposite direction. It is present both in

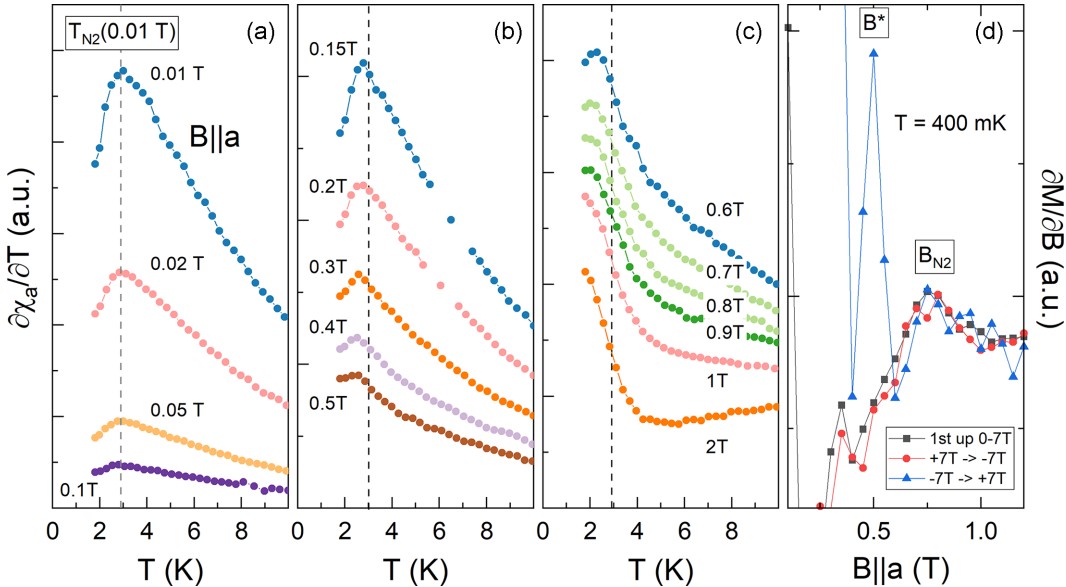


FIG. 13. Anomalies associated with  $T_{N2}(B)$ : [(a)–(c)] Temperature derivative of the static magnetic susceptibility,  $\partial\chi_a/\partial T$  for various fields  $B \parallel a$  axis, at low temperatures. Ordinates cover different scales for visibility. The dashed lines show  $T_{N2}$  at 10 mT. (d) Isothermal magnetic susceptibility  $\partial M/\partial B$  at  $T = 400$  mK for  $B \parallel a$  axis. The data illustrate a field sweep  $0$  T  $\rightarrow$   $7$  T  $\rightarrow$   $-7$  T  $\rightarrow$   $7$  T.  $B_{N2}$  marks a (nonhysteretic) feature associated with the phase boundary of AF III. The anomaly at  $B^*$  only appears after applying high magnetic fields of opposite field direction. For the full sweep see Fig. S10 in the SM [31].

AF III and AF II (see Fig. S11 of the SM). The origin of this anomaly in unclear.

The resulting data points down to 400 mK enclosing the low-temperature phase AF III are summarized in the inset of the phase diagram in Fig. 10(b). In the low-temperature phase AF III, both magnetic sublattices develop long-range magnetic order in agreement to the neutron data from Ref. [37] obtained at 1.5 K in zero magnetic field. The behavior for  $B||c$  is less clear: Although for  $B = 10$  mT applied  $||c$  we observe a slightly broader peak in  $\partial\chi_c/\partial T$  at 3 K as well, this feature disappears already at 50 mT so that the phase boundary cannot be distinguished anymore (see Fig. S17 in the SM).

An additional notable feature of materials with inequivalent sublattices is the potential for a compensation point which appears in  $\text{SmCrO}_3$  at  $T_{\text{comp}} = 6$  K. It is induced by the antiparallel alignment of  $R^{3+}$  and transition metal ion  $M^{3+}$  magnetic moments, as demonstrated, e.g., in  $\text{GdCrO}_3$  ( $T_{\text{comp}} = 144$  K, 100 Oe) [68,69],  $\text{ErFeO}_3$  ( $T_{\text{comp}} = 46$  K, 100 Oe) [70,71],  $\text{SmFeO}_3$  ( $T_{\text{comp}} = 3.9$  K, 300 Oe) [24,72],  $\text{NdFeO}_3$  ( $T_{\text{comp}} = 7.6$  K, 100 Oe) [23], or  $n$   $\alpha$ - $\text{Cr}_3(\text{PO}_4)_2$  ( $T_{\text{comp}} = 5$  K, 1000 Oe) [73]. A theoretical approach by Yamaguchi describes interactions between  $R^{3+}$  and  $\text{Cr}^{3+}$  moments by a temperature-dependent anisotropic effective field acting mainly on the  $\text{Cr}^{3+}$  moments and following the direction of the net magnetic component of the  $\text{Cr}^{3+}$  sublattice [26]. Application of external magnetic field yields a competing energy scale to the temperature-dependent internal field which explains the observed complex field dependencies typically observed in two-sublattice systems such as  $\text{Dy}_{0.5}\text{Pr}_{0.5}\text{FeO}_3$  [74],  $\text{YFeO}_3$  [75],  $\text{GdFeO}_3$  [76], or  $\text{ErCrO}_3$  [77].

#### IV. SUMMARY

We present the high-pressure optical floating-zone growth of  $\text{SmCrO}_3$  single crystals and the investigation of  $\text{SmCrO}_3$  magnetic phase diagrams. This study reports, for the first time, the experimental parameters for the growth of  $\text{SmCrO}_3$  single crystals using the floating-zone method. Access to high-quality single crystals enables us to study the magnetic phase diagrams for the different field directions and to clarify the complex magnetism in  $\text{SmCrO}_3$  arising from the interplay of anisotropic 3d and 4f magnetic sublattices.

Long-range order of the sublattices appears at  $T_N = 192$  K and  $T_{N2} = 3$  K, respectively. In contrast to previous reports on polycrystals, our single-crystal data imply a discontinuous and one-step spin-reorientation of net magnetic moments from the  $c$  axis into the  $ab$  plane at zero magnetic field at  $T_{\text{SR}} = 33$  K. Its discontinuous nature is maintained if  $B$  is applied  $||c$

axis. Our analysis indicates that the spin configuration is  $\Gamma_4$  for  $T > T_{\text{SR}}$ , while it is dominated by  $\Gamma_2$  for  $T < T_{\text{SR}}$ . Our single-crystal study in particular rules out that the collinear antiferromagnetic structure  $\Gamma_1$  may be realized in AF II below 10 K as reported in Ref. [41] but confirms a considerable uncompensated moment in the spin-reoriented phases AF II and AF III. While the presence of a net magnetic moment in principle is consistent with the  $\Gamma_2$  configuration as suggested in Ref. [38], we find clear deviations from the  $\Gamma_2$  behavior. In addition, while the size of the net magnetic moment decreases on cooling below  $\sim 20$  K, the interplay of the two magnetic sublattices also results in a temperature variation of the in-plane net magnetic moment at  $T_{N2}$  when long-range  $\text{Sm}^{3+}$  magnetic order evolves and the AF III phase is established. For AF III, our data suggest but do not unambiguously prove the presence of a small remaining moment  $||c$ ; the observation that the in-plane angle  $\alpha$  is still finite, however, suggests that the  $\Gamma_2$  configuration not realized in AF III either.

When applying finite magnetic fields, notably, we find a triple point as well as tricritical behavior for  $B||a$  axis which further highlights the complex interplay of anisotropic magnetic moments in  $\text{SmCrO}_3$ . The magnetic phase diagrams of  $\text{SmCrO}_3$  for fields along all crystallographic directions down to 0.4 K and up to 14 T provide a crucial foundation for future detailed investigations of the complex magnetic interactions and magnetoelectric coupling in orthochromites.

#### ACKNOWLEDGMENTS

Support by Deutsche Forschungsgemeinschaft (DFG) under Germany's Excellence Strategy EXC2181/1-390900948 (The Heidelberg STRUCTURES Excellence Cluster) is gratefully acknowledged. N.Y. acknowledges fellowship by the Chinese Scholarship Council (File No. 201906890005). L.B. acknowledges funding by the German Research Foundation (DFG) via Research Training Group GRK 2948/1. The authors thank Ilse Glass, Siegmar Roth, and Andre Beck for technical support of x-ray diffraction.

#### DATA AVAILABILITY

The data that support the findings of this article are not publicly available. The data are available from the authors on reasonable request.

The supplemental material contains further information on the grown crystal, x-ray diffraction, and magnetization data as well as the phase diagram for fields  $||b$  axis, including reference [78].

---

- [1] J. Herbst, R2Fe14B materials: Intrinsic properties and technological aspects, *Rev. Mod. Phys.* **63**, 819 (1991).
- [2] M. Sagawa, S. Hirosawa, H. Yamamoto, S. Fujimura, and Y. Matsuura, Nd–Fe–B permanent magnet materials, *Jpn. J. Appl. Phys.* **26**, 785 (1987).
- [3] R. Perkins and S. Strässler, Interpretation of the magnetic properties of pseudobinary  $\text{Sm}_2(\text{Co},M)_{17}$  compounds. I. Magnetocrystalline anisotropy, *Phys. Rev. B* **15**, 477 (1977).
- [4] K. Buschow, Intermetallic compounds of rare-earth and 3d transition metals, *Rep. Prog. Phys.* **40**, 1179 (1977).
- [5] J. M. Coey, *Magnetism and Magnetic Materials* (Cambridge University Press, Cambridge, UK, 2010).
- [6] A. Kimel, A. Kirilyuk, A. Tsvetkov, R. Pisarev, and T. Rasing, Laser-induced ultrafast spin reorientation in the antiferromagnet  $\text{TmFeO}_3$ , *Nature (Lond)* **429**, 850 (2004).

[7] K. Yamaguchi, T. Kurihara, Y. Minami, M. Nakajima, and T. Suemoto, Terahertz time-domain observation of spin reorientation in orthoferrite  $\text{ErFeO}_3$  through magnetic free induction decay, *Phys. Rev. Lett.* **110**, 137204 (2013).

[8] H. Maeter, H. Luetkens, Y. G. Pashkevich, A. Kwadrin, R. Khasanov, A. Amato, A. A. Gusev, K. V. Lamonova, D. A. Chervinskii, R. Klingeler, C. Hess, G. Behr, B. Büchner, and H.-H. Klauss, Interplay of rare earth and iron magnetism in  $r\text{FeAsO}$  ( $r$  = La, Ce, Pr, and Sm): Muon-spin relaxation study and symmetry analysis, *Phys. Rev. B* **80**, 094524 (2009).

[9] Y. Su, J. Zhang, L. Li, B. Li, Y. Zhou, D. Deng, Z. Chen, and S. Cao, Temperature dependence of magnetic properties and change of specific heat in perovskite  $\text{ErCrO}_3$  chromites, *Appl. Phys. A* **100**, 73 (2010).

[10] E. A. Popova, D. V. Volkov, A. N. Vasiliev, A. A. Demidov, N. P. Kolmakova, I. A. Gudim, L. N. Bezmaternykh, N. Tristan, Y. Skourski, B. Büchner, C. Hess, and R. Klingeler, Magnetization and specific heat of  $\text{TbFe}_3(\text{BO}_3)_4$ : Experiment and crystal-field calculations, *Phys. Rev. B* **75**, 224413 (2007).

[11] E. A. Popova, N. Tristan, A. N. Vasiliev, V. L. Temerov, L. N. Bezmaternykh, N. Leps, B. Büchner, and R. Klingeler, Magnetization and specific heat of  $\text{DyFe}_3(\text{BO}_3)_4$  single crystal, *Eur. Phys. J. B* **62**, 123 (2008).

[12] X. Qian, L. Chen, S. Cao, and J. Zhang, A study of the spin reorientation with t-e orbital hybridization in  $\text{SmCrO}_3$ , *Solid State Commun.* **195**, 21 (2014).

[13] U. Stockert, N. Leps, L. Wang, G. Behr, S. Wurmehl, B. Büchner, and R. Klingeler, Pr magnetism and its interplay with the Fe spin-density wave in  $\text{PrFeAsO}_{1-x}f_x$  ( $x = 0, 0.15$ ), *Phys. Rev. B* **86**, 144407 (2012).

[14] S. Artyukhin, M. Mostovoy, N. P. Jensen, D. Le, K. Prokes, V. G. De Paula, H. N. Bordallo, A. Maljuk, S. Landsgesell, H. Ryll *et al.*, Solitonic lattice and Yukawa forces in the rare-earth orthoferrite  $\text{TbFeO}_3$ , *Nat. Mater.* **11**, 694 (2012).

[15] M. C. Weber, M. Guennou, D. M. Evans, C. Toulouse, A. Simonov, Y. Kholina, X. Ma, W. Ren, S. Cao, M. A. Carpenter *et al.*, Emerging spin-phonon coupling through cross-talk of two magnetic sublattices, *Nat. Commun.* **13**, 443 (2022).

[16] Y. Tokunaga, Y. Taguchi, T.-H. Arima, and Y. Tokura, Electric-field-induced generation and reversal of ferromagnetic moment in ferrites, *Nat. Phys.* **8**, 838 (2012).

[17] Y. Tokunaga, N. Furukawa, H. Sakai, Y. Taguchi, T.-H. Arima, and Y. Tokura, Composite domain walls in a multiferroic perovskite ferrite, *Nat. Mater.* **8**, 558 (2009).

[18] U. Adem, L. Wang, D. Fausti, W. Schottenhamel, P. H. M. van Loosdrecht, A. Vasiliev, L. N. Bezmaternykh, B. Büchner, C. Hess, and R. Klingeler, Magnetodielectric and magnetoelastic coupling in  $\text{TbFe}_3(\text{BO}_3)_4$ , *Phys. Rev. B* **82**, 064406 (2010).

[19] E. Hassanpour, M. C. Weber, Y. Zemp, L. Kürten, A. Bortis, Y. Tokunaga, Y. Taguchi, Y. Tokura, A. Cano, T. Lottermoser *et al.*, Interconversion of multiferroic domains and domain walls, *Nat. Commun.* **12**, 2755 (2021).

[20] Y. Su, L. Li, Z. Xing, Z. Feng, D. Deng, B. Kang, S. Cao, and J. Zhang, Study of magnetism and specific-heat properties for multiferroic  $\text{YCrO}_3$  chromites, in *Proceedings of the International Symposium on Applications of Ferroelectrics (ISAF/PFM) and International Symposium on Piezoresponse Force Microscopy and Nanoscale Phenomena in Polar Materials* (IEEE, Los Alamitos, CA, 2011), pp. 1–4.

[21] J.-S. Zhou, J. A. Alonso, V. Pomjakushin, J. B. Goodenough, Y. Ren, J.-Q. Yan, and J.-G. Cheng, Intrinsic structural distortion and superexchange interaction in the orthorhombic rare-earth perovskites  $\text{RCrO}_3$ , *Phys. Rev. B* **81**, 214115 (2010).

[22] J. R. Sahu, C. R. Serrao, and C. Rao, Modification of the multiferroic properties of  $\text{YCrO}_3$  and  $\text{LuCrO}_3$  by Mn substitution, *Solid State Commun.* **145**, 52 (2008).

[23] S. J. Yuan, W. Ren, F. Hong, Y. B. Wang, J. C. Zhang, L. Bellaiche, S. X. Cao, and G. Cao, Spin switching and magnetization reversal in single-crystal  $\text{NdFeO}_3$ , *Phys. Rev. B* **87**, 184405 (2013).

[24] S. Cao, H. Zhao, B. Kang, J. Zhang, and W. Ren, Temperature induced spin switching in  $\text{SmFeO}_3$  single crystal, *Sci. Rep.* **4**, 5960 (2014).

[25] S. Huang, G. Zerihun, Z. Tian, S. Yuan, G. Gong, C. Yin, and L. Wang, Magnetic exchange bias and high-temperature giant dielectric response in  $\text{SmCrO}_3$  ceramics, *Ceram. Int.* **40**, 13937 (2014).

[26] T. Yamaguchi, Theory of spin reorientation in rare-earth orthochromites and orthoferrites, *J. Phys. Chem. Solids* **35**, 479 (1974).

[27] I. Dzyaloshinsky, A thermodynamic theory of “weak” ferromagnetism of antiferromagnetics, *J. Phys. Chem. Solids* **4**, 241 (1958).

[28] T. Moriya, Anisotropic superexchange interaction and weak ferromagnetism, *Phys. Rev.* **120**, 91 (1960).

[29] A. Moskvin, Dzyaloshinskii-Moriya coupling in 3d insulators, *Condens. Matter* **4**, 84 (2019).

[30] R. Hornreich, Magnetic interactions and weak ferromagnetism in the rare-earth orthochromites, *J. Magn. Magn. Mater.* **7**, 280 (1978).

[31] See Supplemental Material at <http://link.aps.org/supplemental/10.1103/PhysRevB.111.174437> which contains further information on the grown crystal and magnetization data.

[32] S. Mishra, Keerthana, K. Rudrapal, B. Jana, K. P. Islam, A. Sagdeo, A. R. Chaudhuri, V. Adyam, and D. Choudhury, Structural origin of room-temperature ferroelectricity in spark-plasma sintered  $\text{DyCrO}_3$  and  $\text{LaCrO}_3$ , *Phys. Rev. B* **107**, 214104 (2023).

[33] B. Rajeswaran, D. I. Khomskii, A. K. Zvezdin, C. N. R. Rao, and A. Sundaresan, Field-induced polar order at the Néel temperature of chromium in rare-earth orthochromites: Interplay of rare-earth and Cr magnetism, *Phys. Rev. B* **86**, 214409 (2012).

[34] K. R. S. Preethi Meher, A. Wahl, A. Maignan, C. Martin, and O. I. Lebedev, Observation of electric polarization reversal and magnetodielectric effect in orthochromites: A comparison between  $\text{LuCrO}_3$  and  $\text{ErCrO}_3$ , *Phys. Rev. B* **89**, 144401 (2014).

[35] S. Das, R. K. Dokala, B. Weise, P. K. Mishra, R. Medwal, R. S. Rawat, and S. Thota, Phonon scattering and magnetic manifold switching in  $(\text{GdSm})\text{CrO}_3$ , *Phys. Rev. Mater.* **7**, 084410 (2023).

[36] S. Yano, C.-W. Wang, Y. Zhu, K. Sun, and H.-F. Li, Magnetic structure and phase transition in a single crystal of  $\text{ErCrO}_3$ , *Phys. Rev. B* **108**, 174406 (2023).

[37] P. Gupta and P. Poddar, Study of magnetic and thermal properties of  $\text{SmCrO}_3$  polycrystallites, *RSC Adv.* **6**, 82014 (2016).

[38] T. Sau, P. Yadav, S. Sharma, R. Raghunathan, P. Manuel, V. Petricek, U. P. Deshpande, and N. P. Lalla, High-resolution time of flight neutron diffraction and magnetization studies of spin

reorientation and polar transitions in  $\text{SmCrO}_3$ , *Phys. Rev. B* **103**, 144418 (2021).

[39] T. Sau, S. Sharma, P. Yadav, R. Baumbach, T. Siegrist, A. Banerjee, and N. P. Lalla, First-order nature of the spin-reorientation phase transition in  $\text{SmCrO}_3$ , *Phys. Rev. B* **106**, 064413 (2022).

[40] M. Tripathi, R. Choudhary, and D. Phase, Phase coexistence and the magnetic glass-like phase associated with the Morin type spin reorientation phase transition in  $\text{SmCrO}_3$ , *RSC Adv.* **6**, 90255 (2016).

[41] M. Tripathi, R. J. Choudhary, D. M. Phase, T. Chatterji, and H. E. Fischer, Evolution of magnetic phases in  $\text{SmCrO}_3$ : A neutron diffraction and magnetometric study, *Phys. Rev. B* **96**, 174421 (2017).

[42] M. Tripathi, T. Chatterji, H. E. Fischer, R. Raghunathan, S. Majumder, R. J. Choudhary, and D. M. Phase, Role of local short-scale correlations in the mechanism of negative magnetization, *Phys. Rev. B* **99**, 014422 (2019).

[43] N. E. Massa, K. Holldack, R. Sopracase, V. Ta Phuoc, L. del Campo, P. Echegut, and J. A. Alonso, Identification of spin wave resonances and crystal field levels in simple chromites  $RCrO_3$  ( $R = \text{Pr, Sm, Er}$ ) at low temperatures in the THz spectral region, *J. Magn. Magn. Mater.* **468**, 294 (2018).

[44] S. Schneider, R. Roth, and J. Waring, Solid state reactions involving oxides of trivalent cations, *J. Res. Natl. Bur. Stand. Sec. A Phys. Chem.* **65**, 345 (1961).

[45] C. Neef, H. Wadeppohl, H.-P. Meyer, and R. Klingeler, High-pressure optical floating-zone growth of  $\text{Li}(\text{Mn, Fe})\text{PO}_4$  single crystals, *J. Cryst. Growth* **462**, 50 (2017).

[46] N. Yuan, High-Pressure Single Crystal Growth and Magnetization Studies on Correlated Electron Systems, Ph.D. thesis, Heidelberg University (2024).

[47] Rigaku Oxford Diffraction Ltd, Yarnton, Oxfordshire, E 2015 CrysAlis PRO.

[48] G. M. Sheldrick, A short history of *SHELX*, *Acta Cryst. A* **64**, 112 (2008).

[49] G. M. Sheldrick, Crystal structure refinement with *SHELXL*, *Acta Cryst. C* **71**, 3 (2015).

[50] V. Petříček, M. Dušek, and L. Palatinus, Crystallographic computing system JANA2006: General features, *Z. Kristallogr.* **229**, 345 (2014).

[51] N. Wizent, G. Behr, W. Löser, B. Büchner, and R. Klingeler, Challenges in the crystal growth of  $\text{Li}_2\text{CuO}_2$  and  $\text{LiMnPo}_4$ , *J. Cryst. Growth* **318**, 995 (2011).

[52] D. Prabhakaran and A. Boothroyd, Crystal growth of spin-ice pyrochlores by the floating-zone method, *J. Cryst. Growth* **318**, 1053 (2011).

[53] W. Hergett, C. Neef, H. Wadeppohl, H.-P. Meyer, M. M. Abdel-Hafiez, C. Ritter, E. Thauer, and R. Klingeler, High-pressure optical floating-zone growth of  $\text{Li}_2\text{FeSiO}_4$  single crystals, *J. Cryst. Growth* **515**, 37 (2019).

[54] S. Koohpayeh, D. Fort, and J. Abell, The optical floating zone technique: A review of experimental procedures with special reference to oxides, *Prog. Cryst. Growth Charact. Mater.* **54**, 121 (2008).

[55] J. L. Schmehr, M. Aling, E. Zoglin, and S. D. Wilson, High-pressure laser floating zone furnace, *Rev. Sci. Instrum.* **90**, 043906 (2019).

[56] K. Dey, W. Hergett, P. Telang, M. M. Abdel-Hafiez, and R. Klingeler, Magnetic properties of high-pressure optical floating-zone grown  $\text{LaNiO}_3$  single crystals, *J. Cryst. Growth* **524**, 125157 (2019).

[57] J. Rodríguez-Carvajal, Recent advances in magnetic structure determination by neutron powder diffraction, *Physica B: Condens. Matter* **192**, 55 (1993).

[58] Y. Su, J. Zhang, B. Li, B. Kang, Q. Yu, C. Jing, and S. Cao, The dependence of magnetic properties on temperature for rare earth  $\text{ErCrO}_3$  chromites, *Ceram. Int.* **38**, S421 (2012).

[59] J. Ding, L. Wen, H. Li, H. Hao, and Y. Zhang, Ferroelectric and magnetoelectric origins of multiferroic  $\text{SmCrO}_3$ , *J. Am. Ceram. Soc.* **102**, 267 (2019).

[60] A. Ghosh, K. Dey, M. Chakraborty, S. Majumdar, and S. Giri, Polar octahedral rotations, cation displacement and ferroelectricity in multiferroic  $\text{SmCrO}_3$ , *Europhys. Lett.* **107**, 47012 (2014).

[61] A. McDannald, L. Kuna, M. S. Seehra, and M. Jain, Magnetic exchange interactions of rare-earth-substituted  $\text{DyCrO}_3$  bulk powders, *Phys. Rev. B* **91**, 224415 (2015).

[62] S. Yin, M. S. Seehra, C. J. Guild, S. L. Suib, N. Poudel, B. Lorenz, and M. Jain, Magnetic and magnetocaloric properties of  $\text{HoCrO}_3$  tuned by selective rare-earth doping, *Phys. Rev. B* **95**, 184421 (2017).

[63] T. H. K. Barron and G. K. White, *Heat Capacity and Thermal Expansion at Low Temperatures*, The International Cryogenic Monograph Series (Kluwer Academic/Plenum Publishers, Amsterdam, 1999).

[64] Y. B. Bazaliy, L. T. Tsymbal, G. N. Kakazei, A. I. Izotov, and P. E. Wigen, Spin-reorientation in  $\text{ErFeO}_3$ : Zero-field transitions, three-dimensional phase diagram, and anisotropy of erbium magnetism, *Phys. Rev. B* **69**, 104429 (2004).

[65] S. Mishra, K. P. Islam, and D. Choudhury, Extrinsic origin of spontaneous exchange-bias and negative magnetization: A case study on  $\text{SmCrO}_3$  and  $\text{DyCrO}_3$ , *J. Magn. Magn. Mater.* **603**, 172220 (2024).

[66] R. Klingeler, B. Büchner, S.-W. Cheong, and M. Hücker, Weak ferromagnetic spin and charge stripe order in  $\text{La}_{5/3}\text{Sr}_{1/3}\text{NiO}_4$ , *Phys. Rev. B* **72**, 104424 (2005).

[67] G. Gorodetsky, R. Hornreich, S. Shaft, B. Sharon, A. Shaulov, and B. Wanklyn, Second-order nature of the spin-reorientation phase transition in  $\text{SmCrO}_3$ , *Phys. Rev. B* **16**, 515 (1977).

[68] L. Yin, J. Yang, X. Kan, W. Song, J. Dai, and Y. Sun, Giant magnetocaloric effect and temperature induced magnetization jump in  $\text{GdCrO}_3$  single crystal, *J. Appl. Phys.* **117**, 133901 (2015).

[69] I. Fita, R. Puzniak, A. Wisniewski, and V. Markovich, Spin switching and unusual exchange bias in the single-crystalline  $\text{GdCrO}_3$  compensated ferrimagnet, *Phys. Rev. B* **100**, 144426 (2019).

[70] X. Ma, W. Fan, G. Zhao, H. Chen, C. Wang, B. Kang, Z. Feng, J.-Y. Ge, W. Ren, and S. Cao, Low field control of spin switching and continuous magnetic transition in an  $\text{ErFeO}_3$  single crystal, *Phys. Chem. Chem. Phys.* **24**, 735 (2022).

[71] R. Huang, S. Cao, W. Ren, S. Zhan, B. Kang, and J. Zhang, Large rotating field entropy change in  $\text{ErFeO}_3$  single crystal with angular distribution contribution, *Appl. Phys. Lett.* **103**, 162412 (2013).

[72] L. G. Marshall, J.-G. Cheng, J.-S. Zhou, J. B. Goodenough, J.-Q. Yan, and D. G. Mandrus, Magnetic coupling between  $\text{Sm}^{3+}$  and the canted spin in an antiferromagnetic  $\text{SmFeO}_3$  single crystal, *Phys. Rev. B* **86**, 064417 (2012).

[73] A. N. Vasiliev, O. S. Volkova, E. Hammer, R. Glaum, J.-M. Broto, M. Millot, G. Nénert, Y. T. Liu, J.-Y. Lin, R. Klingeler, M. Abdel-Hafiez, Y. Krupskaya, A. U. B. Wolter, and B. Büchner, Weak ferrimagnetism and multiple magnetization reversal in  $\alpha$ -Cr<sub>3</sub>(PO<sub>4</sub>)<sub>2</sub>, *Phys. Rev. B* **85**, 014415 (2012).

[74] H. Wu, S. Cao, M. Liu, Y. Cao, B. Kang, J. Zhang, and W. Ren, Twofold spin reorientation and field-induced incomplete phase transition in single-crystal Dy<sub>0.5</sub>Pr<sub>0.5</sub>FeO<sub>3</sub>, *Phys. Rev. B* **90**, 144415 (2014).

[75] X. Lin, J. Jiang, Z. Jin, D. Wang, Z. Tian, J. Han, Z. Cheng, and G. Ma, Terahertz probes of magnetic field induced spin reorientation in YFeO<sub>3</sub> single crystal, *Appl. Phys. Lett.* **106**, 092403 (2015).

[76] M. Das, S. Roy, and P. Mandal, Giant reversible magnetocaloric effect in a multiferroic GdFeO<sub>3</sub> single crystal, *Phys. Rev. B* **96**, 174405 (2017).

[77] K. Toyokawa, S. Kurita, and K. Tsushima, Spectroscopic study of the field-induced spin reorientation in ErCrO<sub>3</sub>, *Phys. Rev. B* **19**, 274 (1979).

[78] R. White, Review of recent work on the magnetic and spectroscopic properties of the rare-earth orthoferrites, *J. Appl. Phys.* **40**, 1061 (1969).